

Nanoscale visualization and spectral fingerprints of the charge order in ScV_6Sn_6 distinct from other kagome metals

Siyu Cheng^{1,*}, Zheng Ren^{2,*}, Hong Li¹, Ji Seop Oh^{3,2}, Hengxin Tan⁴, Ganesh Pokharel⁵, Jonathan M. DeStefano⁶, Elliott Rosenberg⁶, Yucheng Guo², Yichen Zhang², Ziqin Yue^{2,13}, Yongbin Lee⁷, Sergey Gorovikov⁸, Marta Zonno⁸, Makoto Hashimoto⁹, Donghui Lu⁹, Liqin Ke⁷, Federico Mazzola^{10,11}, Junichiro Kono², R. J. Birgeneau^{3,12}, Jiun-Haw Chu⁶, Stephen D. Wilson⁵, Ziqiang Wang¹, Binghai Yan⁴, Ming Yi^{2,&} and Ilija Zeljkovic^{1,^}

¹*Department of Physics, Boston College, Chestnut Hill, MA 02467, USA*

²*Department of Physics and Astronomy, Rice University, Houston, TX 77005, USA*

³*Department of Physics, University of California, Berkeley, CA 94720, USA*

⁴*Department of Condensed Matter Physics, Weizmann Institute of Science, Rehovot, Israel*

⁵*Materials Department, University of California Santa Barbara, Santa Barbara, California 93106, USA*

⁶*Department of Physics, University of Washington, Seattle, Washington 98195, USA*

⁷*Ames Laboratory, Ames, IA, 50011, USA*

⁸*Canadian Light Source, Inc., 44 Innovation Boulevard, Saskatoon SK S7N 2V3, Canada*

⁹*Stanford Synchrotron Radiation Lightsource, SLAC National Accelerator Laboratory, Menlo Park, California 94025, USA*

¹⁰*Istituto Officina dei Materiali (IOM)–CNR, Laboratorio TASC, Area Science Park, S.S.14, km 163.5, I-34149 Trieste, Italy*

¹¹ *Department of Molecular Sciences and Nanosystems, Ca' Foscari University of Venice, 30172 Venice, Italy*

¹²*Materials Science Division, Lawrence Berkeley National Laboratory, Berkeley, CA 94720, USA*

¹³*Applied Physics Graduate Program, Smalley-Curl Institute, Rice University, Houston, TX 77005, USA*

**contributed equally*

Corresponding authors: my32@rice.edu[&] and ilija.zeljkovic@bc.edu[^]

Abstract

Charge density waves (CDWs) have been tied to a number of unusual phenomena in kagome metals, including rotation symmetry breaking, time-reversal symmetry breaking and superconductivity. The majority of the experiments in kagome metals thus far have focused on the CDW states in AV_3Sb_5 ($A=\text{K}, \text{Cs}, \text{Rb}$) and FeGe , characterized by the $2a_0$ by $2a_0$ CDW period in the kagome plane. Recently, a bulk CDW phase ($T_{\text{CDW}} \approx 92$ K) with an entirely different wave length and orientation has been reported in ScV_6Sn_6 , as the first realization of a CDW state in the broad RM_6X_6 crystal structure. Here, using a combination of scanning tunneling microscopy/spectroscopy and angle-resolved photoemission spectroscopy, we reveal the microscopic structure and the spectroscopic signatures of this charge ordering phase in ScV_6Sn_6 . Differential conductance dI/dV spectra show a partial gap opening in the density-of-states of about 20 meV at the Fermi level. This is much smaller than the spectral gaps observed in AV_3Sb_5 and FeGe despite the comparable T_{CDW} temperatures in these systems, suggesting substantially weaker coupling strength in ScV_6Sn_6 . Surprisingly, despite the three-dimensional bulk

nature of the charge order, we find that the charge modulation is only observed on the kagome termination. Temperature-dependent band structure evolution suggests a modulation of the surface states as a consequence of the emergent charge order, with an abrupt spectral weight shift below T_{CDW} consistent with the first-order phase transition. The similarity of the electronic band structures of ScV_6Sn_6 and TbV_6Sn_6 (where the charge ordering is absent), together with the first-principle calculations, suggests that charge ordering in ScV_6Sn_6 may not be primarily electronically driven. Interestingly, in sharp contrast to the CDW state of cousin AV_3Sb_5 , we find no evidence supporting rotation symmetry breaking. Our results reveal a distinctive nature of the charge ordering phase in ScV_6Sn_6 in comparison to other kagome metals.

Introduction

The kagome lattice, a pattern of tessellated hexagons connected by small corner-sharing triangles, emerged as a versatile platform for exploring a variety of novel quantum phases of matter. Due to the geometric frustration intrinsic to the kagome lattice, layered kagome materials are characterized by a characteristic electronic band structure consisting of Dirac fermions, flat bands and Van Hove singularities (VHSs) ¹⁻⁵. This prototypical band structure can be intertwined with a rich array of exotic electronic instabilities, which have been theoretically explored and experimentally realized in several families of kagome metals thus far. For example, Fe- ⁶⁻¹⁵, Mn-¹⁶⁻²¹ and Co- ²²⁻²⁵ based kagome magnets yielded the realization of topological flat bands ^{11,23,26}, Dirac and Weyl fermions ^{6,9,12,22,24,27} and Fermi arcs ^{22,24}; a non-magnetic V-based AV_3Sb_5 ($A=\text{Cs, K, Rb}$) kagome metal family ²⁸⁻³⁰ on the other hand attracted a large interest ³¹⁻⁴¹ due to the emergence of superconductivity and various symmetry-breaking states potentially in connection to loop current orders ⁴².

The recently discovered bilayer kagome metals in the RV_6Sn_6 structure (“166” family), where R stands for a rare earth ion, offer a new tunable platform to investigate Fermi surface instabilities of the kagome lattice ⁴³⁻⁴⁸. Similarly to that in AV_3Sb_5 , vanadium atoms that comprise the kagome layers in RV_6Sn_6 remain non-magnetic ^{44-46,49}, but magnetism can still be selectively tuned by the choice of the rare earth element R ⁴⁹⁻⁵¹. Out of the wide array of kagome metals in the RV_6Sn_6 structure, ScV_6Sn_6 presents a unique platform where a charge density wave (CDW) state was reported below $T_{\text{CDW}} \approx 92 \text{ K}$ ⁴⁶. Similar to the bulk CDW phase in AV_3Sb_5 that is three-dimensional, this charge ordering (CO) phase in ScV_6Sn_6 is also three-dimensional but with a different wave vector $\mathbf{Q}^* = (1/3, 1/3, 1/3)$. Understanding the formation of the CO and how it compares to the more intensely investigated CDW in AV_3Sb_5 has been of high interest, but very little is known about the origin and the spectroscopic fingerprint of the charge order in ScV_6Sn_6 .

Here we use a combination of scanning tunneling microscopy/spectroscopy (STM/S) and angle-resolved photoemission spectroscopy (ARPES) to investigate the electronic structure and the CO formation in ScV_6Sn_6 . STM topographs reveal a $\sqrt{3} \times \sqrt{3} R30^\circ$ electronic superstructure, which corresponds to the in-plane component of the bulk CO wavevector identified in diffraction measurements. We visualize the three-dimensional nature of the CO by imaging the expected phase offset across different terraces. Interestingly, the microscopic signature of the CO at the surface is termination-dependent – while a small, partial spectral gap at the Fermi level and the CO peaks are observed on the kagome termination, both are notably absent on the Sn termination. In contrast to the C_2 -symmetric CDW state in AV_3Sb_5 , we discover that the rotational symmetry in the CO state of ScV_6Sn_6 appears to be preserved. Our low-temperatures ARPES measurements reveal that the electronic structures of ScV_6Sn_6 (with the CO) share

much in common with that of TbV_6Sn_6 (without the CO). Lastly, we uncover the temperature evolution of the electronic bands in the vicinity of the K-point, which is consistent with the modulation of the surface bands in first-principle calculations as a consequence of the CO.

Results

Microscopic visualization of the CO structure

Crystal structure of ScV_6Sn_6 is composed of layers of V atoms arranged on a kagome network, each stacked between a ScSn^3 layer and a $\text{Sn}^1\text{-Sn}^2\text{-Sn}^1$ trilayer (Fig. 1a,b). We cleave bulk single crystals of ScV_6Sn_6 in ultra-high vacuum to expose a pristine surface before measurements (Methods). Related materials in the same crystal structure tend to cleave along the c -axis to reveal ab -plane surface terminations^{19,20,27,43,45,47}. This is consistent with the observed surface structure of UHV-cleaved ScV_6Sn_6 – STM topographs exhibit a hexagonal lattice (Fig. 1e-h) and the occasionally observed steps are an integer number of c -axis unit cell heights (Fig. 1c, Fig. 3). STM topographs show two types of surface morphologies, both with a hexagonal lattice (Fig. 1e,g, Supplementary Figure 1, Supplementary Figure 2). We identify the termination in Fig. 1e as the Sn^2 termination due to the clearly resolved individual atoms forming a hexagonal lattice (top inset in Fig. 1e) similar to the Sn^2 surface imaged in YMn_6Sn_6 ²⁰. The surface termination in Fig. 1g is likely the kagome layer, as we deem the other two possibilities, Sn^1 and ScSn^3 , to be unlikely: the Sn^1 termination in YMn_6Sn_6 showed a triangular atomic structure²⁰ and the ReSn^3 surface appears to have a tendency to reconstruct into stripe-like features as reported in TbMn_6Sn_6 ²⁷.

In addition to the atomic Bragg peaks $\mathbf{Q}_{\text{Bragg}}^i$ ($i=a, b$ or c), Fourier transforms (FTs) of STM topographs of the V kagome termination show six additional superlattice peaks (Fig. 1h). These FT peaks are positioned exactly along each Γ -K direction at $\mathbf{Q}^* = (\mathbf{Q}_{\text{Bragg}}^i + \mathbf{Q}_{\text{Bragg}}^j)/3$ ($i, j = a, b$ or c) and are symmetric with respect to the center of the FT. They correspond to the staggered intensity modulations seen in real-space in STM topographs (inset in Fig. 1g). To investigate the origin of these modulations, we examine the energy dependence of the associated wave vectors in the FTs of differential conductance $dI/dV(\mathbf{r}, V)$ maps. The FT peaks are discernable in a wide range of energies $e\cdot V$ and the peak positions in momentum-transfer space are independent of the bias V . Moreover, the peak position is exactly consistent with the in-plane component of the newly discovered CO phase detected in diffraction experiments⁴⁶. Therefore, the charge modulations observed in the STM topograph in Fig. 1g represent a microscopic visualization of the bulk CO state at the surface of this system. Differential conductance dI/dV spectra on the kagome surface termination show a gap-like feature, with a partial suppression in the density-of-states of about 20 meV, approximately symmetric with respect to the Fermi level (Fig. 2e). As the CO is the only known ordered state in this system, we deem that the gap is likely related to the emergent CO.

To gain insight into the three-dimensional nature of the order revealed to have a $(1/3, 1/3, 1/3)$ wave vector from diffraction measurements⁴⁶, we study the charge modulations across a step edge (Fig. 3). Our theoretical calculations suggest that structural distortions from the CO create an effective $(2\pi/3, 2\pi/3)$ phase shift between the adjacent kagome bilayers (Fig. 3b). As the structural distortion is in principle intimately tied to the charge modulation pattern observed in STM measurements, one would also expect to observe an apparent charge modulation phase shift between adjacent atomic terraces. To explore this, we study in detail an STM topograph between two different terraces (Fig. 3c). Both terraces are terminated by the vanadium layer and show the same CDW pattern that can be clearly resolved in real space (Fig. 3c). By tracking the positions of the charge modulation peaks on the upper terraces, we observe

a phase shift of the equivalent modulations peaks on the lower terrace (Fig. 3c). This is consistent with the expected bulk CO structure (Fig. 3b), thus providing the first microscopic insight into the three-dimensional nature of the CO that persists at the surface of the material.

Absence of rotational symmetry breaking in the CO state of ScV₆Sn₆

In the CDW phase of AV₃Sb₅, an array of experimental techniques observed signatures of in-plane rotational symmetry breaking, which first onsets at the T_{CDW} temperature^{38,52,53} and reduces the in-plane rotational symmetry from six-fold to two-fold^{31,32,36,38,52–54}. We proceed to explore whether the rotational symmetry of the kagome bilayer in ScV₆Sn₆ is also broken. For pedagogical purposes, we first discuss the experiments on KV₃Sb₅. Similarly to the analysis done in Refs.^{36,52,54}, we compare the CDW amplitudes along the three inequivalent directions as a function of energy (Fig. 4c). A noticeable difference in the CDW amplitude dispersions is clearly observed between different peaks, with one direction being markedly different from the other two that are nearly the same. This FT peak anisotropy is also reflected in the unidirectionality of the pattern in $dI/dV(r,V)$ maps (Fig. 4d). In ScV₆Sn₆ however, we find that the shape of the CO amplitude dispersions versus energy along the three directions is nearly identical (Fig. 4a). We note that tiny differences between the three curves reflect the measurement and analysis uncertainty, as well as the inevitable small STM tip anisotropy. The approximately rotationally symmetric CO signature can also be seen in representative $dI/dV(r,V)$ maps (Fig. 4b). These measurements suggest the absence of rotation symmetry breaking in the CO state of ScV₆Sn₆.

Spectroscopic investigation of the nature of the CO

Having identified the real-space signatures of the CO in ScV₆Sn₆, we next turn to the momentum-space evidence. ARPES has been an extremely useful tool in determining the signature kagome bands^{14,41,55–58}, the CDW gap modulation and the band reconstruction associated with CDW order^{57–59} in AV₃Sb₅ and FeGe where CDWs have been reported thus far. We first show the measured Fermi surface (FS) of ScV₆Sn₆ obtained on the kagome termination (see Supplementary Note 1, Supplementary Figure 3). The FS consists of segments connecting the M points of the Brillouin zone (BZ) (Fig. 5a), similar to that of other kagome metals such as AV₃Sb₅^{29,41,57,59} and FeGe^{14,58}. From the dispersions measured along the high symmetry direction Γ -K-M, we observe a quadratic band centered at Γ , with the band bottom located at about 1 eV below the Fermi level, E_F . This band extends to the M point in the form of a VHS near E_F (Fig. 5c). This is consistent with the typical band structure associated with the kagome lattice, and also matches well with the band structure calculated by the density-functional theory (DFT) (Fig. 5d), suggesting weak electron-electron correlation effects. Since both ScV₆Sn₆ and TbV₆Sn₆ share the same V kagome layer, we proceed to compare the band structures of the two systems. Both the FS and band dispersions show a striking similarity. In particular, the locations of the VHS at M are very close to E_F in both systems, with that in ScV₆Sn₆ slightly below E_F and that in TbV₆Sn₆ slightly above E_F (Fig. 5c,g). The small difference in VHS positions is also consistent with the DFT calculations (Fig. 5d,h).

To investigate the effect of the CO on the electronic structure of ScV₆Sn₆, we perform temperature-dependent measurements of dispersions along the Γ -K-M direction across the transition $T^* \approx 92$ K⁴⁶. To reveal the band reconstruction, we present a series of normalized intensity plots, showing the subtracted difference between the cuts taken at selected temperatures and that taken at 120 K $> T^*$ (Fig. 6b) (see Supplementary Figure 4). The most substantial difference appears in the vicinity of the K points near E_F , seen as patches of blue on these color maps, and disappears above about 100 K (Fig. 6b). This difference

can also be clearly seen by comparing the energy distribution curves (EDCs) taken at 20 K and 120 K in the region across the K point, where we discover a prominent spectral weight shift towards E_F on the side of the K point closer to the M point (upper half of Fig. 6c). The temperature evolution of the spectral weight change can also be seen in the collapsed stack of integrated EDCs in this momentum-space region (Fig. 6d). To quantitatively determine the temperature dependence of the spectral weight shift, we plot the peak area of this EDC integrated between -0.2 V and E_F (Fig. 6d,e). The peak area decreases as the temperature increases, with an abrupt drop across T^* (Fig. 6e), consistent with the transition observed. The abrupt drop of the peak area is compatible with the first-order nature of the phase transition⁴⁶.

To understand the origin of the band reconstruction near the K points, we perform DFT calculations for the CDW state. We first present the DFT calculations for the bulk bands along Γ -K-M (Fig. 6f). Note that the CDW band structure has been unfolded back into the pristine BZ for ease of comparison. Comparing the pristine and CDW calculations, we observe little difference near the K point. This can be understood as the three-dimensional CDW wavevector $(1/3, 1/3, 1/3)$ corresponds to a reduction of the pristine BZ to a smaller one, where the pristine K and $K'_{1/3}$ (the point at $1/3$ along K' - H') points are now equivalent in the reconstructed BZs (Fig. 6h). However, DFT calculations for bulk states predict no states in the vicinity of H point near E_F in the pristine phase (Supplementary Figure 5, Methods), which would lead to negligible folding between K and $K'_{1/3}$ points. Hence, the band reconstruction we observe near the K point is unlikely to be directly due to bulk band folding. However, when the surface states are subject to the CDW folding potential, they would fulfill the in-plane folding condition $\mathbf{Q}^*_{\text{in-plane}} = (\mathbf{Q}^a_{\text{Bragg}} + \mathbf{Q}^b_{\text{Bragg}})/3$, folding states between the K' and K points. We carried out DFT calculations for the surface states on the kagome termination under the bulk CDW wavevector $(1/3, 1/3, 1/3)$. Indeed, folded bands and gap openings appear near the K point (Fig. 6g). Specifically, immediately below E_F at K, a band crossing opens a gap and the upper branch is pushed towards E_F (blue arrow in Fig. 6g). This is consistent with the spectral weight shift towards E_F we observe at the K point (Fig. 6i).

Discussion

Our experiments provide the first microscopic visualization of the CO phase in ScV_6Sn_6 and its spectroscopic fingerprints. The spectral gap observed in dI/dV spectra is about 20 meV, which is much smaller than the CDW gap observed in dI/dV spectra of AV_3Sb_5 and FeGe of about 40-50 meV^{31,35,36,60}, despite the comparable T_{CDW} temperatures in the two systems. This indicates a substantially weaker coupling in the CO state of ScV_6Sn_6 compared to AV_3Sb_5 . While charge modulations are clearly observed on the kagome termination, we note that Sn^2 surface termination does not show the CO in either the topograph or $dI/dV(\mathbf{r}, V)$ maps near E_F . Correspondingly, the small spectral gap in dI/dV spectra on the kagome termination is notably absent on the Sn termination (Fig. 2e,f). These observations should be highly relevant for other surface sensitive studies, which should take into account the unusual termination dependence of the bulk order in this system. For comparison, the 2×2 CDW state in AV_3Sb_5 can be detected in STM/S measurements of both surface terminations imaged^{31,32,35,36}.

Our results also suggest that while the CO in ScV_6Sn_6 breaks the translational symmetry of the lattice, the rotational symmetry of the kagome bilayer is preserved. This is again in contrast to AV_3Sb_5 , where rotation symmetry breaking occurs concomitant with the CDW onset^{38,52,53}. It is conceivable that rotation symmetry breaking in AV_3Sb_5 is related to the unusual orbital picture as recently evidenced in isostructural CsTi_3Bi_5 ^{61,62}.

Finally, we comment on the role of VHSs in ScV₆Sn₆ in comparison to other kagome metals. The VHSs have now been observed at the M points of the BZ near E_F in both ScV₆Sn₆ and TbV₆Sn₆, as well as AV₃Sb₅ and FeGe. In AV₃Sb₅ and FeGe, it is natural to relate the 2 x 2 CDW order to the FS nesting as the wavevector in principle fulfills the nesting condition. However, in the present case of ScV₆Sn₆, while the vHSs remain close to E_F at the M point, the CO wavevector is no longer compatible with the same FS nesting wavevectors. Hence, we deem that the CO in ScV₆Sn₆ may not be primarily electronically driven. This is further supported by the similarities in the fermiology of ScV₆Sn₆ and TbV₆Sn₆, and the contrasting presence of the CO in the former and the absence in the latter. In the case of ScV₆Sn₆, DFT calculations of the phonon spectra also indicate the presence of phonon softening at the K point of the BZ⁶³. Interestingly, recent Monte Carlo simulations revealed the importance of the proximity of a Dirac point to E_F in stabilizing the $\sqrt{3} \times \sqrt{3}$ CDW order on a kagome lattice⁶⁴, a condition that appears to be satisfied in our system (Fig. 5). In the larger context of kagome metals, our observations suggest that the nesting of VHSs may be a contributor but not the sole driver of the CO, and the combination of the favorable Dirac cone placement near E_F and phonon softening at K could play an important role here. Overall, the charge modulation observed in ScV₆Sn₆ is likely to be more akin to the lattice-driven structural transition often associated with first order phase transitions rather than the conventional electronically-driven CDW order associated with a second order phase transitions.

In conclusion, we provide both spatial- and momentum-resolved evidence of the unusual CO in ScV₆Sn₆. We observe a $\sqrt{3} \times \sqrt{3}$ R30° superstructure by STM that corresponds to the in-plane component of the CO wavevector $Q^* = (1/3, 1/3, 1/3)$, as well as a phase shift across an atomic step edge that is consistent with the reported 3D CO periodicity along the *c*-axis. We find the rotation symmetry to be preserved in the CO state of ScV₆Sn₆ in sharp contrast to the C₂-symmetric CDW in AV₃Sb₅ (A=Cs, K, Rb) family. In momentum space, we observe the presence of the signature VHSs near the M point of the BZ near E_F, yet band reconstruction across T* to occur dominantly near the K points of the BZ, compatible with the folding vector of Q* of surface bands. The similarity of the electronic structure of ScV₆Sn₆ and TbV₆Sn₆ where the ordering is absent strongly suggests a non-electronic origin of the CO in ScV₆Sn₆. Taken all evidence together, our results reveal a distinctive nature of the CO in ScV₆Sn₆ in comparison to other kagome metals.

Methods

Single crystal growth and characterization. Single crystals of ScV₆Sn₆ were grown from Sc (pieces, 99.9%), V (pieces, 99.7%), and Sn (shots, 99.99%) via a flux-based growth technique. The flux mixture of Sc, V and Sn was loaded inside an alumina crucible with a molar ratio of 1:6:40 and then heated at 1125°C for 12 h. Then, the mixture was cooled at a rate of 2°C/hr to 780°C and centrifuged to separate the single crystals from the excess Sn-flux.

STM experiments. Single crystals of ScV₆Sn₆ were cleaved in ultrahigh vacuum and inserted into the STM head at 4.5 K. All STM measurements were taken at about 4.5 K, using home-made electrochemically etched tungsten tips annealed in UHV before STM experiments. STM data were acquired using a customized Unisoku USM1300 STM system. Spectroscopic measurements were made using a standard lock-in technique with 910-Hz frequency and bias excitation as noted in the figure captions.

Angle-resolved photoemission spectroscopy (ARPES) experiments. ARPES measurements on ScV₆Sn₆ were performed at the QMSC beamline of the Canadian Light Source, equipped with a R4000 electron analyzer,

and TbV_6Sn_6 at Stanford Synchrotron Radiation Lightsource (SSRL), Beamline 5-2, equipped with a DA30 electron analyzer. The single crystals were cleaved *in-situ* at 20 K and measured in ultra-high vacuum with a base pressure better than 6×10^{-11} Torr. Energy and angular resolution were set to be better than 20 meV and 0.1° , respectively (Supplementary Figure 6).

Density-functional theory (DFT) calculations. All calculations are performed within the DFT implemented in the Vienna ab-initio Simulation Package (VASP)⁶⁵. The generalized gradient approximation as parameterized by Perdew, Burke, and Ernzerhof⁶⁶ is employed for the exchange-correlation interaction between electrons. The energy cutoff for the plane wave basis set is 300 eV. A force convergence criteria of $1 \text{ meV}/\text{\AA}$ is used in the structural relaxation. The bulk Brillouin zone of the pristine ScV_6Sn_6 is sampled with a k -mesh of $21 \times 21 \times 10$. The surface states of both the pristine phase and the CDW phase are simulated with slabs of 8 kagome layers thick, and obtained by projecting the slab band structure onto the surface unit cell. Spin-orbital coupling is considered for the bulk band structure while not considered in slab calculations.

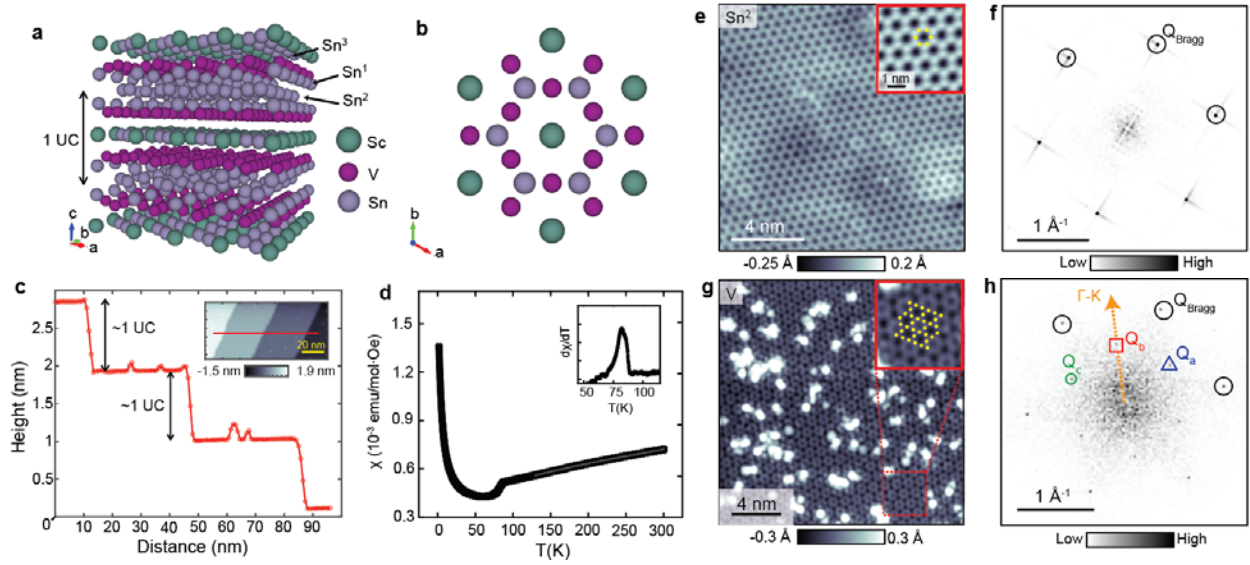


Figure 1. Crystal structure, magnetization and topographic characterization of ScV_6Sn_6 . (a) The schematic of the bulk crystal structure of ScV_6Sn_6 , and (b) ab -plane surface atomic structure. (c) Topographic linecut showing single steps between consecutive Sn^2 terraces taken along the red line in the inset. Inset in (c) shows an STM topograph spanning several consecutive steps. (d) Magnetization measurements (zero-field cooled, then taken at 1 T applied in the ab -plane warming up) showing a kink at T^* associated with the bulk transition. STM topographs of (e) Sn^2 termination and (g) kagome termination, and (f, h) associated Fourier transforms. Atomic Bragg peaks are circled in green; CO peaks are enclosed in blue circles, red squares and orange triangles. STM setup conditions: (c) $I_{\text{set}} = 10$ pA, $V_{\text{sample}} = 1$ V; (e) $I_{\text{set}} = 400$ pA, $V_{\text{sample}} = 20$ mV; (g) $I_{\text{set}} = 200$ pA, $V_{\text{sample}} = 200$ mV.

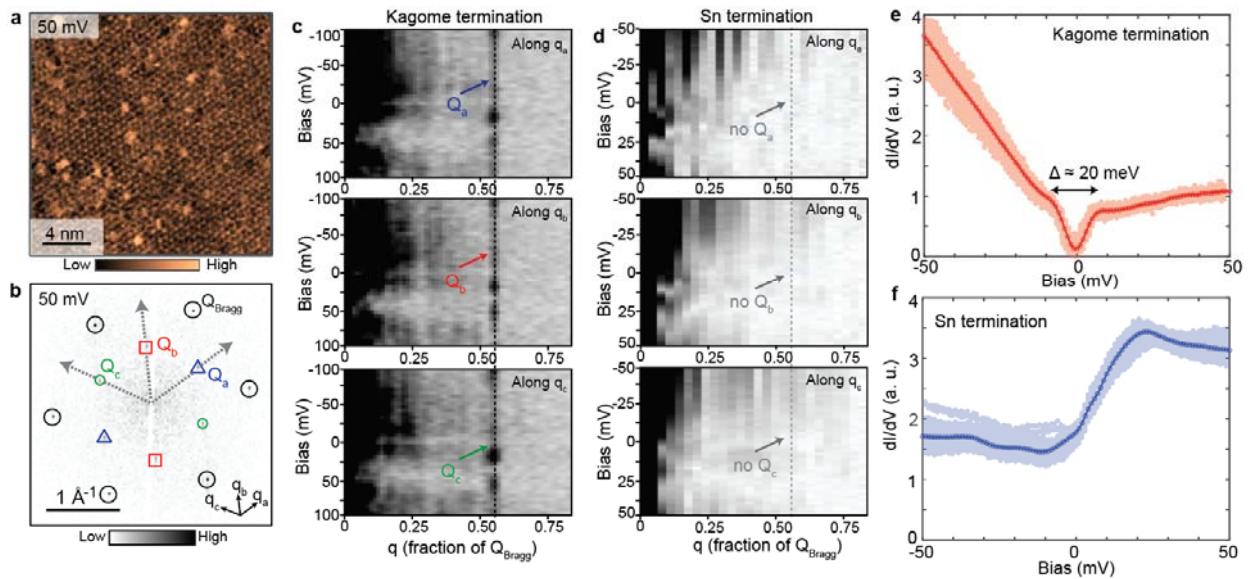


Figure 2. Termination-dependent scanning tunneling microscopy and spectroscopy of the CO state. (a) Differential conductance $dI/dV(r, V=50 \text{ mV})$ map acquired over the kagome termination, and (b) associated Fourier transform (FT). (c) Energy-dependent FT linecuts of $dI/dV(r, V)$ maps of the kagome termination, starting at the FT center along the three Γ -K directions (labeled as q_a , q_b and q_c in panel (b)). Non-dispersive CO peaks are observed along all three directions. (d) Energy-dependent FT linecuts of $dI/dV(r, V)$ maps of the Sn^2 termination, starting at the FT center along the three Γ -K directions. No additional peaks are observed at the same momentum-transfer position where the CO peaks are seen on the kagome termination. (e,f) Average dI/dV spectra (solid line and circle symbols) over (e) the kagome and (f) Sn^2 termination. Diffuse orange (blue) background shows representative dI/dV spectra taken over several linecuts in the same field-of-view on kagome (Sn^2) surface. STM setup conditions: (a) $I_{\text{set}} = 50 \text{ pA}$, $V_{\text{sample}} = 50 \text{ mV}$, $V_{\text{exc}} = 4 \text{ mV}$; (c) $I_{\text{set}} = 30 \text{ pA}$, $V_{\text{sample}} = -100 \text{ mV}$, $V_{\text{exc}} = 5 \text{ mV}$; (d) $I_{\text{set}} = 200 \text{ pA}$, $V_{\text{sample}} = 50 \text{ mV}$, $V_{\text{exc}} = 2 \text{ mV}$; (e) $I_{\text{set}} = 30 \text{ pA}$, $V_{\text{sample}} = 50 \text{ pA}$, $V_{\text{exc}} = 3 \text{ mV}$; (f) $I_{\text{set}} = 200 \text{ pA}$, $V_{\text{sample}} = 50 \text{ mV}$, $V_{\text{exc}} = 1 \text{ mV}$.

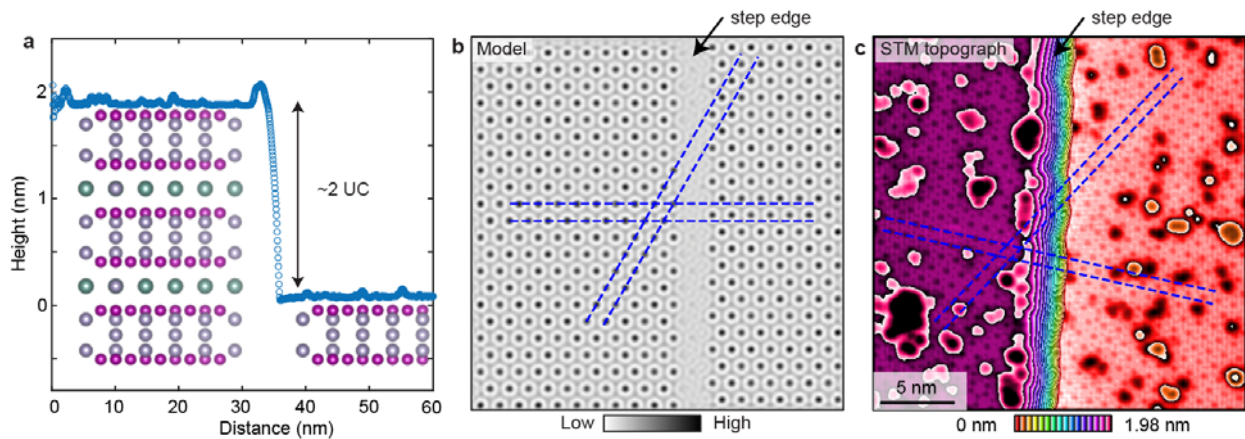


Figure 3. Visualizing the three-dimensional nature of the CO in ScV_6Sn_6 . (a) Schematic of the two unit cell step between two kagome-terminated terraces. (b) Simulated CO morphology across the step in (a). Red lines in (b) trace the peaks of the charge modulations on the left half of the image; peaks on the right sides of the image are noticeably offset from the red lines, highlighting the phase shift between the two. (c) STM topograph of the step shown in (a). Similarly to panel (b), yellow lines trace the peaks of the charge modulations on the upper (left) terrace; the charge modulation peaks on the right side (lower terrace) are again visibly away from these lines, demonstrating a phase offset between the two qualitatively consistent with (b). STM setup condition: (a,c) $I_{\text{set}} = 100 \text{ pA}$, $V_{\text{sample}} = 1 \text{ V}$.

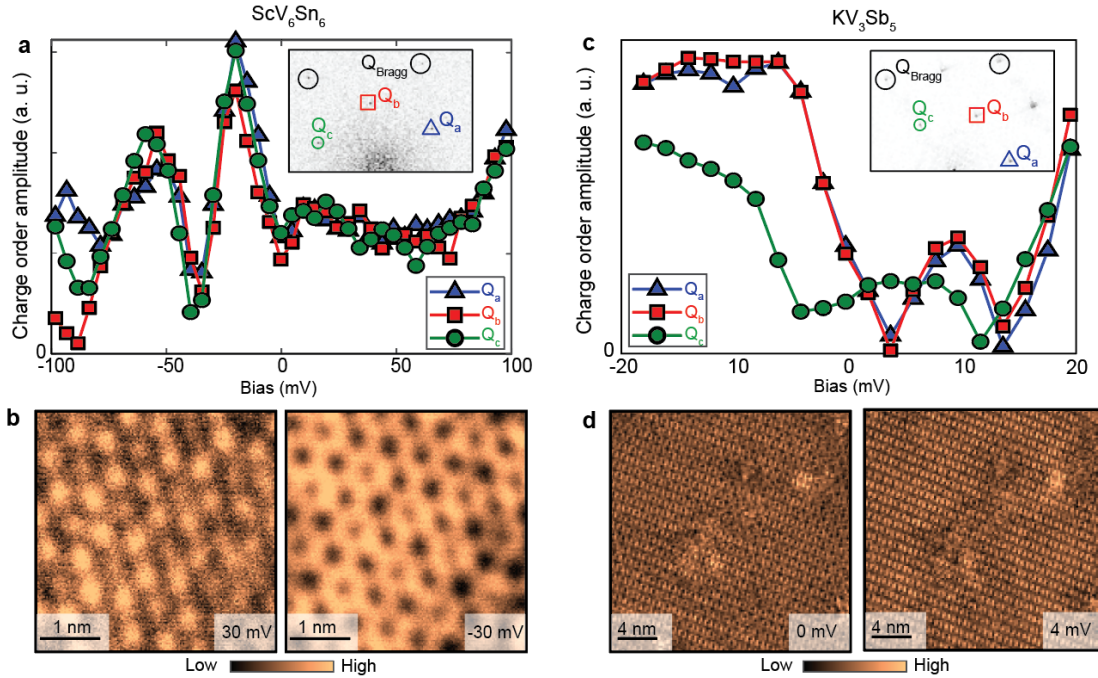


Figure 4. Scanning tunneling microscopy and spectroscopy investigation of rotation symmetry breaking in ScV_6Sn_6 , and the comparison to KV_3Sb_5 . (a) Energy-dependent amplitudes of the three inequivalent CDW peaks (marked in the example Fourier transform in the inset) in ScV_6Sn_6 . The overall shape of all three dispersion curves is nearly identical and largely overlaps one another. (b) Zoom-in on representative high-resolution $dI/dV(r, V)$ maps showing the approximately rotationally symmetric real-space signature. (c) Energy-dependent amplitudes of the three inequivalent CDW peaks (marked in the example Fourier transform in the inset) in cousin kagome metal KV_3Sb_5 . the dispersion of Q_c amplitude is noticeably different than the other two, Q_a and Q_b , that are nearly indistinguishable. (d) Representative $dI/dV(r, V)$ maps showing a unidirectional real-space signature that breaks the six-fold symmetry. STM setup conditions: (a) $I_{\text{set}} = 30 \text{ pA}$, $V_{\text{sample}} = -100 \text{ mV}$, $V_{\text{exc}} = 5 \text{ mV}$; (b) $I_{\text{set}} = 100 \text{ pA}$, $V_{\text{sample}} = 100 \text{ mV}$, $V_{\text{exc}} = 2 \text{ mV}$; (c,d) $I_{\text{set}} = 150 \text{ pA}$, $V_{\text{sample}} = 10 \text{ mV}$, $V_{\text{exc}} = 1 \text{ mV}$.

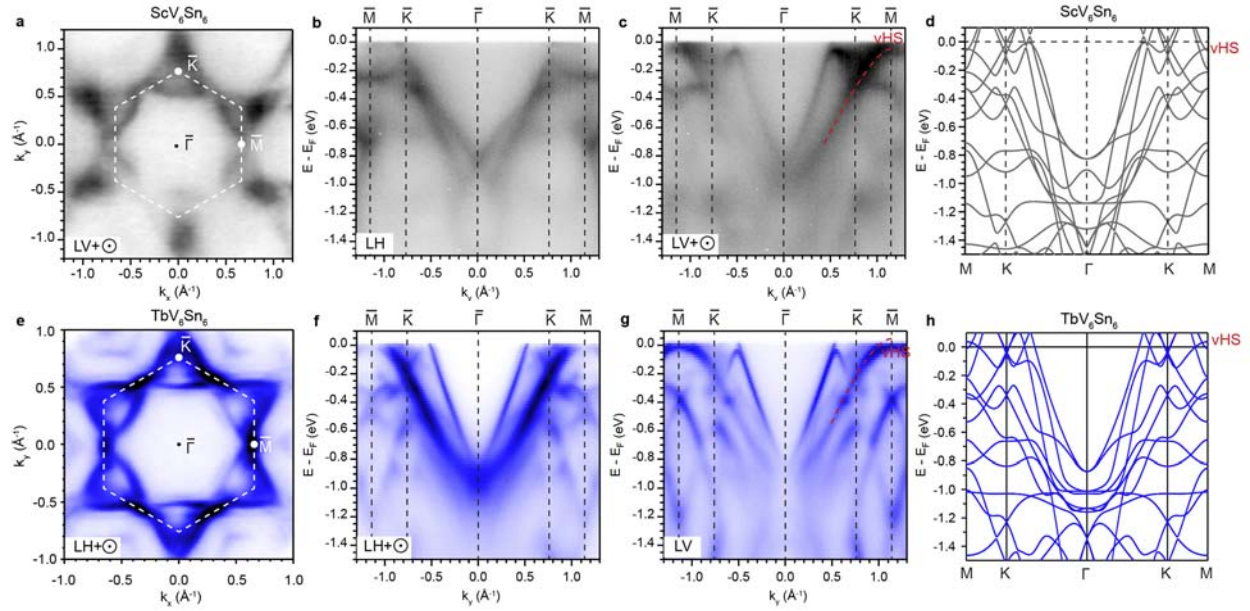


Figure 5. Comparison between band structure of ScV_6Sn_6 and TbV_6Sn_6 . **a** Fermi surface map of ScV_6Sn_6 overlaid with the 2D BZ. **b,c** Dispersions acquired along the high-symmetry direction Γ -K-M, with the polarization LH and LV+ \odot , respectively. Here LH and LV are defined as the in-plane component along the horizontal and vertical directions of the image. When there is an out-of-plane contribution due to experimental setup, we denote it by “+ \odot ”. The red dashed line serves as a guide to the eye for the band forming the VHS near E_F . **d** Band structure of ScV_6Sn_6 in the pristine phase calculated by DFT. **e-h** Data (83 eV photon energy) and DFT calculations of TbV_6Sn_6 corresponding to each panel of ScV_6Sn_6 above.

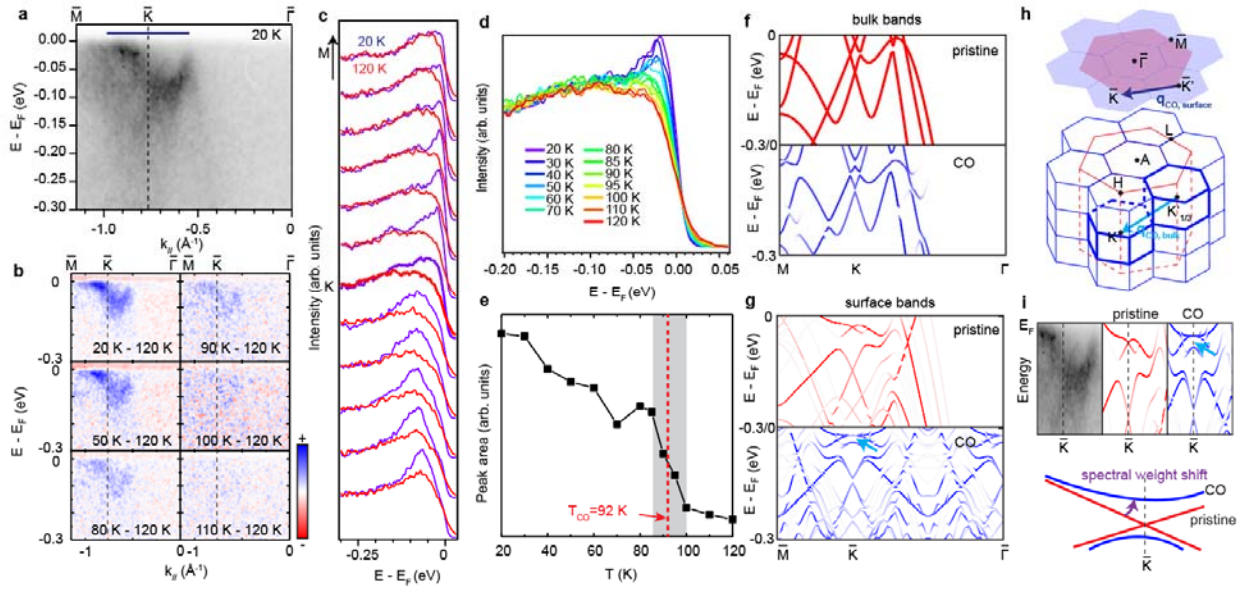


Figure 6. Temperature-dependent band reconstruction induced by the CO. **a** Γ -K-M cut in the vicinity of E_F taken at 20 K. **b** Subtraction between cuts measured at selected temperatures and that at 120 K, with the energy and momentum range same as **a**. The intensity is such that white represents zero, indicating no change. **c** EDC comparison taken at 20 K and 120 K in the region denoted by the dark blue bar in **a**. **d** Stacked EDCs as a function of temperature acquired in the region between K and M. **e** Integrated peak area of each curve in **d** between -0.2 eV and E_F , plotted as a function of temperature. Grey shade covers the temperature range where an abrupt drop of peak area occurs. The red dashed line indicates T^* . **f** Bulk band structure calculated by DFT, in the pristine phase (upper) and the CO phase (lower). **g** Surface bands in the pristine and the CO phase calculated by DFT. The blue arrow points to the gap opening (see text). **h** Schematic of the surface and bulk BZs. Dark blue and light blue arrows correspond to $\mathbf{q}_{\text{CO,surface}}$ and $\mathbf{q}_{\text{CO,bulk}}$, respectively. **i** Direct comparison of ARPES data, pristine surface bands and the surface bands in the CO state, and the schematic showing the origin of the spectral weight shift.

References

1. Sachdev, S. Kagome- and triangular-lattice Heisenberg antiferromagnets: Ordering from quantum fluctuations and quantum-disordered ground states with unconfined bosonic spinons. *Phys. Rev. B* **45**, 12377–12396 (1992).
2. Guo, H.-M. & Franz, M. Topological insulator on the kagome lattice. *Phys. Rev. B* **80**, 113102 (2009).
3. Mazin, I. I. *et al.* Theoretical prediction of a strongly correlated Dirac metal. *Nat. Commun.* **5**, 4261 (2014).
4. Tang, E. & Fu, L. Strain-induced partially flat band, helical snake states and interface superconductivity in topological crystalline insulators. *Nat. Phys.* **10**, 964–969 (2014).
5. Neupert, T., Santos, L., Chamon, C. & Mudry, C. Fractional Quantum Hall States at Zero Magnetic Field. *Phys. Rev. Lett.* **106**, 236804 (2011).
6. Ye, L. *et al.* Massive Dirac fermions in a ferromagnetic kagome metal. *Nature* **555**, 638–642 (2018).
7. Yin, J.-X. X. *et al.* Giant and anisotropic many-body spin–orbit tunability in a strongly correlated kagome magnet. *Nature* **562**, 91–95 (2018).
8. Ye, L. *et al.* de Haas-van Alphen effect of correlated Dirac states in kagome metal Fe₃Sn₂. *Nat. Commun.* **10**, 4870 (2019).
9. Kang, M. *et al.* Dirac fermions and flat bands in the ideal kagome metal FeSn. *Nat. Mater.* **19**, 163–169 (2020).
10. Lin, Z. *et al.* Dirac fermions in antiferromagnetic FeSn kagome lattices with combined space inversion and time-reversal symmetry. *Phys. Rev. B* **102**, 155103 (2020).
11. Lin, Z. *et al.* Flatbands and Emergent Ferromagnetic Ordering in Fe₃Sn₂ Kagome Lattices. *Phys. Rev. Lett.* **121**, 096401 (2018).
12. Ren, Z. *et al.* Plethora of tunable Weyl fermions in kagome magnet Fe₃Sn₂ thin films. *npj Quantum Mater.* **7**, 109 (2022).
13. Chen, T. *et al.* Large anomalous Nernst effect and nodal plane in an iron-based kagome ferromagnet. *Sci. Adv.* **8**, 1–8 (2022).
14. Teng, X. *et al.* Discovery of charge density wave in a kagome lattice antiferromagnet. *Nature* **609**, 490–495 (2022).
15. Li, H. *et al.* Spin-polarized imaging of the antiferromagnetic structure and field-tunable bound states in kagome magnet FeSn. *Sci. Rep.* **12**, 14525 (2022).
16. Zhang, H. *et al.* Topological magnon bands in a room-temperature kagome magnet. *Phys. Rev. B* **101**, 100405 (2020).
17. Wang, Q. *et al.* Field-induced topological Hall effect and double-fan spin structure with a c-axis component in the metallic kagome antiferromagnetic compound YMn₆Sn₆. *Phys. Rev. B* **103**, 014416 (2021).

18. Ghimire, N. J. *et al.* Competing magnetic phases and fluctuation-driven scalar spin chirality in the kagome metal YMn_6Sn_6 . *Sci. Adv.* **6**, eabe2680 (2020).
19. Li, M. *et al.* Dirac cone, flat band and saddle point in kagome magnet YMn_6Sn_6 . *Nat. Commun.* **12**, 3129 (2021).
20. Li, H. *et al.* Manipulation of Dirac band curvature and momentum-dependent g factor in a kagome magnet. *Nat. Phys.* **18**, 644–649 (2022).
21. Ma, W. *et al.* Rare Earth Engineering in RMn_6Sn_6 (R=Gd–Tm, Lu) Topological Kagome Magnets. *Phys. Rev. Lett.* **126**, 246602 (2021).
22. Morali, N. *et al.* Fermi-arc diversity on surface terminations of the magnetic Weyl semimetal $\text{Co}_3\text{Sn}_2\text{S}_2$. *Science* **365**, 1286–1291 (2019).
23. Yin, J.-X. *et al.* Negative flat band magnetism in a spin–orbit-coupled correlated kagome magnet. *Nat. Phys.* **15**, 443–448 (2019).
24. Liu, D. F. *et al.* Magnetic Weyl semimetal phase in a Kagomé crystal. *Science* **365**, 1282–1285 (2019).
25. Liu, E. *et al.* Giant anomalous Hall effect in a ferromagnetic kagome-lattice semimetal. *Nat. Phys.* **14**, 1125–1131 (2018).
26. Kang, M. *et al.* Topological flat bands in frustrated kagome lattice CoSn . *Nat. Commun.* **11**, 4004 (2020).
27. Yin, J.-X. X. *et al.* Quantum-limit Chern topological magnetism in TbMn_6Sn_6 . *Nature* **583**, 533–536 (2020).
28. Ortiz, B. R. *et al.* New kagome prototype materials: discovery of KV_3Sb_5 , RbV_3Sb_5 and CsV_3Sb_5 . *Phys. Rev. Mater.* **3**, 094407 (2019).
29. Ortiz, B. R. *et al.* CsV_3Sb_5 : A Z_2 Topological Kagome Metal with a Superconducting Ground State. *Phys. Rev. Lett.* **125**, 247002 (2020).
30. Kenney, E. M., Ortiz, B. R., Wang, C., Wilson, S. D. & Graf, M. J. Absence of local moments in the kagome metal KV_3Sb_5 as determined by muon spin spectroscopy. *J. Phys. Condens. Matter* **33**, 235801 (2021).
31. Jiang, Y.-X. *et al.* Unconventional chiral charge order in kagome superconductor KV_3Sb_5 . *Nat. Mater.* **20**, 1353–1357 (2021).
32. Zhao, H. *et al.* Cascade of correlated electron states in the kagome superconductor CsV_3Sb_5 . *Nature* **599**, 216–221 (2021).
33. Guo, C. *et al.* Switchable chiral transport in charge-ordered kagome metal CsV_3Sb_5 . *Nature* **611**, 461–466 (2022).
34. Chen, H. *et al.* Roton pair density wave in a strong-coupling kagome superconductor. *Nature* **599**, 222–228 (2021).
35. Liang, Z. *et al.* Three-Dimensional Charge Density Wave and Surface-Dependent Vortex-Core States in a Kagome Superconductor CsV_3Sb_5 . *Phys. Rev. X* **11**, 031026 (2021).

36. Li, H. *et al.* Rotation symmetry breaking in the normal state of a kagome superconductor KV_3Sb_5 . *Nat. Phys.* **18**, 265–270 (2022).
37. Mielke, C. *et al.* Time-reversal symmetry-breaking charge order in a kagome superconductor. *Nature* **602**, 245–250 (2022).
38. Xu, Y. *et al.* Three-state nematicity and magneto-optical Kerr effect in the charge density waves in kagome superconductors. *Nat. Phys.* **18**, 1470–1475 (2022).
39. Yang, S.-Y. *et al.* Giant, unconventional anomalous Hall effect in the metallic frustrated magnet candidate, KV_3Sb_5 . *Sci. Adv.* **6**, eabb6003 (2020).
40. Wu, X. *et al.* Nature of Unconventional Pairing in the Kagome Superconductors AV_3Sb_5 (A=K, Rb, Cs). *Phys. Rev. Lett.* **127**, 177001 (2021).
41. Kang, M. *et al.* Twofold van Hove singularity and origin of charge order in topological kagome superconductor CsV_3Sb_5 . *Nat. Phys.* **18**, 301–308 (2022).
42. Neupert, T., Denner, M. M., Yin, J.-X., Thomale, R. & Hasan, M. Z. Charge order and superconductivity in kagome materials. *Nat. Phys.* **18**, 137–143 (2022).
43. Peng, S. *et al.* Realizing Kagome Band Structure in Two-Dimensional Kagome Surface States of RV_6Sn_6 (R=Gd, Ho). *Phys. Rev. Lett.* **127**, 266401 (2021).
44. Pokharel, G. *et al.* Electronic properties of the topological kagome metals YV_6Sn_6 and GdV_6Sn_6 . *Phys. Rev. B* **104**, 235139 (2021).
45. Rosenberg, E. *et al.* Uniaxial ferromagnetism in the kagome metal TbV_6Sn_6 . *Phys. Rev. B* **106**, 115139 (2022).
46. Arachchige, H. W. S. *et al.* Charge Density Wave in Kagome Lattice Intermetallic ScV_6Sn_6 . *Phys. Rev. Lett.* **129**, 216402 (2022).
47. Hu, Y. *et al.* Tunable topological Dirac surface states and van Hove singularities in kagome metal GdV_6Sn_6 . *Sci. Adv.* **8**, (2022).
48. Zhang, X. *et al.* Destabilization of the Charge Density Wave and the Absence of Superconductivity in ScV_6Sn_6 under High Pressures up to 11 GPa. *Materials (Basel)*. **15**, 7372 (2022).
49. Pokharel, G. *et al.* Highly anisotropic magnetism in the vanadium-based kagome metal TbV_6Sn_6 . *ArXiv* 2205.15559 (2022).
50. Lee, J. & Mun, E. Anisotropic magnetic property of single crystals RV_6Sn_6 (R=Y, Gd–Tm, Lu). *Phys. Rev. Mater.* **6**, 083401 (2022).
51. Zhang, X. *et al.* Electronic and magnetic properties of intermetallic kagome magnets RV_6Sn_6 (R=Tb–Tm). *Phys. Rev. Mater.* **6**, 105001 (2022).
52. Li, H. *et al.* Unidirectional coherent quasiparticles in the high-temperature rotational symmetry broken phase of AV_3Sb_5 kagome superconductors. *Nat. Phys.* (2023). doi:10.1038/s41567-022-01932-1
53. Xiang, Y. *et al.* Twofold symmetry of c-axis resistivity in topological kagome superconductor CsV_3Sb_5 with in-plane rotating magnetic field. *Nat. Commun.* **12**, 6727 (2021).

54. Nie, L. *et al.* Charge-density-wave-driven electronic nematicity in a kagome superconductor. *Nature* **604**, 59–64 (2022).
55. Luo, J. *et al.* Possible star-of-David pattern charge density wave with additional modulation in the kagome superconductor CsV₃Sb₅. *npj Quantum Mater.* **7**, 30 (2022).
56. Hu, Y. *et al.* Topological surface states and flat bands in the kagome superconductor CsV₃Sb₅. *Sci. Bull.* **67**, 495–500 (2022).
57. Kang, M. *et al.* Charge order landscape and competition with superconductivity in kagome metals. *Nat. Mater.* (2022). doi:10.1038/s41563-022-01375-2
58. Teng, X. *et al.* Intertwined magnetism and charge density wave order in kagome FeGe. *ArXiv* 2210.06653 (2022).
59. Luo, H. *et al.* Electronic nature of charge density wave and electron-phonon coupling in kagome superconductor KV₃Sb₅. *Nat. Commun.* **13**, 273 (2022).
60. Yin, J.-X. *et al.* Discovery of Charge Order and Corresponding Edge State in Kagome Magnet FeGe. *Phys. Rev. Lett.* **129**, 166401 (2022).
61. Li, H. *et al.* Electronic nematicity in the absence of charge density waves in a new titanium-based kagome metal. *Arxiv* 2211.16477 (2022).
62. Yang, H. *et al.* Superconductivity and orbital-selective nematic order in a new titanium-based kagome metal CsTi₃Bi₅. *ArXiv* 2211.12264 (2022).
63. Tan, H. & Yan, B. Abundant lattice instability in kagome metal ScV₆Sn₆. *Arxiv* 2302.07922 (2023).
64. Bradley, O., Cohen-Stead, B., Johnston, S., Barros, K. & Scalettar, R. T. Charge order in the kagome lattice Holstein model: A Hybrid Monte Carlo study. *ArXiv* 2212.05714 (2022).
65. Kresse, G. & Furthmüller, J. Efficiency of ab-initio total energy calculations for metals and semiconductors using a plane-wave basis set. *Comput. Mater. Sci.* **6**, 15–50 (1996).
66. Perdew, J., Burke, K. & Ernzerhof, M. Generalized Gradient Approximation Made Simple. *Phys. Rev. Lett.* **77**, 3865–3868 (1996).

Acknowledgements

S.D.W. and G.P. gratefully acknowledge support via the UC Santa Barbara NSF Quantum Foundry funded via the Q-AMASE-i program under award DMR-1906325. Work at Rice is supported by the U.S. Department of Energy (DOE) grant No. DE-SC0021421 (MY) and the Gordon and Betty Moore Foundation's EPIQS Initiative through grant no. GBMF9470 (MY). Work at the University of California, Berkeley and Lawrence Berkeley National Laboratory was funded by the U.S. DOE, Office of Science, Office of Basic Energy Sciences, Materials Sciences and Engineering Division under Contract No. DE-AC02-05CH11231 (Quantum Materials Program KC2202). This material is based in part upon work supported by the National Science Foundation Graduate Research Fellowship Program under Grant No. DGE-2140004. Part of the research described in this work was performed at the Canadian Light Source, a national research facility of the University of Saskatchewan, which is supported by Canada Foundation for Innovation (CFI), the Natural Sciences and Engineering Research Council of Canada (NSERC), the National Research Council (NRC), the Canadian Institutes of Health Research (CIHR), the Government of Saskatchewan, and the

University of Saskatchewan. This research also used resources of the Stanford Synchrotron Radiation Lightsource, a U.S. DOE Office of Science User Facility under contract No. AC02-76SF00515. Any opinions, findings, and conclusions or recommendations expressed in this material are those of the authors and do not necessarily reflect the views of the National Science Foundation.